Proceedings Paper:
Calmé, B., Kim, S., Morimoto, T.K. et al. (2026) Pressure-free Magnetic Soft Growing Robot with Real-Time Shape Control and Sensing for Biome Sampling. In: Proceedings of 2026 IEEE 9th International Conference on Soft Robotics (RoboSoft). 2026 IEEE 9th International Conference on Soft Robotics (RoboSoft), 07-12 Apr 2026, Kanazawa, Japan. Institute of Electrical and Electronics Engineers (IEEE), pp. 23-29. ISBN: 2769-4526. EISSN: 2769-4534.

https://doi.org/10.1109/robosoft67810.2026.11522898

Pressure-free Magnetic Soft Growing Robot with Real-Time Shape Control and Sensing for Biome Sampling

Benjamin Calmé[1], *Member*, IEEE, Sukjun Kim[2], *Member*, IEEE, Tania K Morimoto[2], *Senior Member*, IEEE, and Pietro Valdastri[1], *Fellow*, IEEE

***Abstract*— Soft growing robots offer a promising solution for deployment in confined and unstructured environments due to their unique locomotion principles. Although this approach has revolutionized the way robots can navigate lumens of varying diameters and shapes, steering these robots remains challenging—especially at bifurcations or when navigating toward specific targets in open-space environments. While ongoing research continues to improve steering capabilities, the shape of soft growing robots is still largely dictated by their surrounding environment. This study addresses this fundamental limitation by extending the concept of magnetic steering previously introduced in the literature. We propose a new approach that employs an embedded magnetic signature to enable full-body shape deformation. Based on a physical model that combines magneto-elasticity with the eversion growth principle, we also introduce a method for shape sensing and demonstrate the concept of pressure-free growth. The robot's magnetic signature is defined along the X and Y axes, while local magnetization along the Z axis enables shape sensing. As a proof of concept, the proposed soft growing robot has a diameter of 1.8 mm and can evert over a length of 6 cm. It incorporates two submillimeter 3D Hall-effect sensors for real-time shape sensing, a camera, and a cytology brush that can be deployed from the inner channel for biome sampling. The robot can grow without internal pressure, be magnetically steered in open space to reach complex configurations such as retroflexion, and its shape can be sensed at frequencies up to 500 Hz.**

I. INTRODUCTION

Soft growing robots constitute a class of soft robotic structures that use eversion as their primary mode of locomotion. They can be described as tube-like systems that elongate from their tips to navigate through tight, cluttered, or unstructured environments without dragging their bodies along. Typically, this is achieved by pressurizing an inverted sleeve so that it everts at the tip, continuously adding new material to the front [1], [2]. This mechanism allows the robot to move forward with minimal friction and gentle contact with its surroundings.

This family of robots has attracted considerable interest due to potential applications in diverse fields, including industrial inspection, search and rescue, and minimally invasive healthcare. Significant research efforts have focused on developing actively steerable and deflectable variants to enhance their maneuverability. Various technical solutions have been proposed for distal tip steering, including pneumatic [3], tendon-driven [4], [5] mechanisms, and, more recently, liquid crystal-based actuation [6]. Although these methods offer active control, they typically require complex tubing or cabling systems connecting actuators and pumps to the distal tip, and face issues such as hysteresis, nonlinearity, and backlash.

In contrast, magnetically steered soft growing robots can overcome many of these limitations [7]. By leveraging the concept of magnetic skins introduced in [8] and the use of hyperelastic materials as described in [9], we investigate the eversion dynamics of a soft growing robot fabricated from an incompressible, isotropic, hyperelastic magnetoelastomer.

Permanent magnets exert forces and torques that act not only on a body as a whole, but also on its constituent material elements, leading to shape changes through magnetoelastic coupling. Magneto-responsive composite materials, soft polymers embedded with micron-scale magnetic particles, enable large elastic deformations under external magnetic fields. Such magnetoelastomeric composites combine the low stiffness and compliance of silicone-based polymers with high magnetic susceptibility. With fine particle dispersion and established fabrication techniques, they offer homogeneous, tunable properties [10], [11]. The nonlinear magneto–mechanical coupling in these materials has opened avenues for device design and material science. This physical intelligence enable applications previously inaccessible to traditional materials.

Although the physics of eversion has been studied for decades [12], [13], its integration into soft growing robot models is often simplified. Prior works have explored localized phenomena such as bulging bifurcations in hyperelastic soft growing robots, but did not fully address the central mechanism of eversion [9]. Here, we re-examine this process to clarify how hyperelastic and magnetoelastic properties interact to define the robot's behavior. Our model demonstrates the feasibility of pressure-free growth, where eversion occurs solely under an applied magnetic field.

We also explore how tailoring the geometry of the inverted material (also called the "tail") can reduce friction between the tail and the everted body. Prior studies have simulated eversion tip geometries [14] and proposed cruciform cross-sections for miniaturization [15] and stiffening [16]. Building

[1]Benjamin Calmé and Pietro Valdastri are with STORM Lab, Institute of Autonomous Systems and Sensing (IRASS), School of Electronic and Electrical Engineering, University of Leeds, UK b.p.calme@leeds.ac.uk

[2]Sukjun Kim and Tania K. Morimoto are with the Department of Mechanical and Aerospace engineering, University of California, San Diego, La Jolla, CA, USA.

This work was supported in part by the Advanced Research and Invention Agency (ARIA) under grant SMRB-SE01-P01 and by the Arnold and Mabel Beckman Foundation (Corresponding author: Benjamin Calmé.)

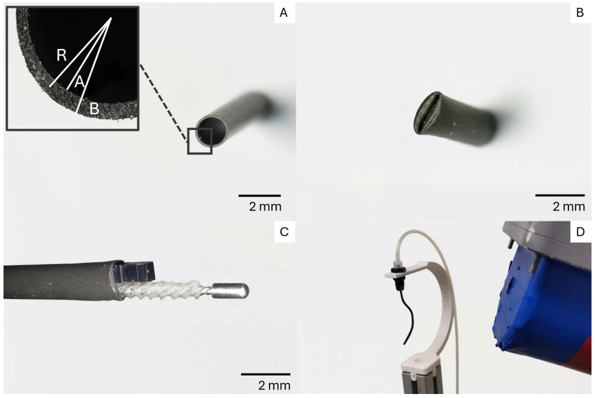

Fig. 1. (A) Fabricated cylindrical body composed of Dragon Skin 10 and NdFeB microparticles. (B) Everting growth mechanism. (C) Functional prototype equipped with a camera and cytology brush. (D) S-shaped deformation achieved by the soft growing robot.

on these findings, we fabricate the robot using a cruciform-shaped magnetoelastic composite and experimentally evaluate the impact of this geometry on friction and structural stiffness.

A robust deformation model is likewise essential for shape sensing. Material properties must be accurately characterized to infer deformation and to avoid ballooning in hyperelastic soft growing robots when pressure is used. Building upon prior work [17], where robot shape was estimated using embedded permanent magnets tracked by Hall-effect sensors, we propose an improved approach. In our design, permanent magnets are replaced by localized markers made from the same hyperelastic polymer but doped with a higher concentration of magnetic particles. These regions are magnetized along an axis orthogonal to the steering direction, enabling accurate, real-time shape sensing along the robot's neutral axis.

This paper presents several key contributions: (i) the development and demonstration—both analytically and experimentally—of the first everting soft growing robot driven without internal pressure, (ii) an innovative tail-molding strategy that reduces friction and enhances structural stiffness, (iii) distributed shape forming along the body, and (iv) real-time shape sensing.

II. Eversion of a Magnetoelastic Soft Growing Robot

A. Deformation Geometry

We model the soft growing robot as an incompressible, isotropic, homogeneous hyperelastic cylindrical tube with reference geometry defined by

$$0 < A \leq R \leq B, \quad 0 \leq \Theta \leq 2\pi, \quad 0 \leq Z \leq L, \qquad (1)$$

in cylindrical coordinates (R, Θ, Z), where A and B are the inner and outer radii, respectively (Fig. 1).

Upon the application of an external input, either a pressure and/or a magnetic field, the cylinder everts, producing a deformed geometry described by

$$0 < a \leq r \leq b, \quad 0 \leq \theta \leq 2\pi, \quad -l \leq z \leq 0, \qquad (2)$$

where (r, θ, z) are the deformed cylindrical coordinates, and a and b are the inner and outer radii of the everted configuration. The inner surface $R = A$ maps to $r = b$, and the outer surface $R = B$ to $r = a$. Assuming no torsion, the azimuthal angle remains constant, $\theta = \Theta$. The deformation gradient $\mathbf{F}$, expressed in cylindrical coordinates, is then

$$\mathbf{F} = \begin{bmatrix} \lambda_r & 0 & 0 \\ 0 & \lambda_\theta & 0 \\ 0 & 0 & \lambda_z \end{bmatrix} = \begin{bmatrix} -\dfrac{dr}{dR} & 0 & 0 \\ 0 & \dfrac{r}{R} & 0 \\ 0 & 0 & \dfrac{z}{Z} \end{bmatrix}. \qquad (3)$$

For an incompressible material, $\det(\mathbf{F}) = 1$, which leads to the equilibrium condition

$$r\lambda_z\lambda_r - R = 0. \qquad (4)$$

From this relation, we obtain

$$r^2 = a^2 + \frac{B^2 - R^2}{\lambda_z}, \quad b^2 = a^2 + \frac{B^2 - A^2}{\lambda_z}. \qquad (5)$$

The deformation equations can then be reduced to a single governing equation expressed in terms of the strain-energy function $W = W(\lambda_r, \lambda_\theta, \lambda_z)$:

$$r\frac{d}{dr}\left(\lambda_r\frac{\partial W}{\partial \lambda_r} - p(r)\right) + \left(\lambda_r\frac{\partial W}{\partial \lambda_r} - p(r)\right) - \left(\lambda_\theta\frac{\partial W}{\partial \lambda_\theta} - p(r)\right) = 0. \qquad (6)$$

Ideally, one would enforce pointwise boundary conditions of zero traction on the outer and inner surfaces of the tube. However, in our case, such conditions are not physically consistent, as they neglect the effects of both friction and magnetic attraction between the everted layers.

B. Governing Equations

In the absence of a magnetic field, the elastomeric material exhibits an isotropic mechanical response, with $H = 0$ and an energy function $W(\mathbf{F}, 0)$ reducing to a purely elastic strain-energy function $w(\lambda_r, \lambda_\theta, \lambda_z)$. This isotropic response depends on the three principal invariants of the right Cauchy–Green deformation tensor $\mathbf{C} = \mathbf{F}^T\mathbf{F}$:

$$\begin{aligned} I_1 &= \mathrm{tr}(\mathbf{C}) = \lambda_r^2 + \lambda_\theta^2 + \lambda_z^2, \\ I_2 &= \frac{1}{2}\left[(\mathrm{tr}\mathbf{C})^2 - \mathrm{tr}(\mathbf{C}^2)\right] = \lambda_r^2\lambda_\theta^2 + \lambda_\theta^2\lambda_z^2 + \lambda_r^2\lambda_z^2, \\ I_3 &= \det(\mathbf{C}) = (\det\mathbf{F})^2 = 1. \end{aligned} \qquad (7)$$

When a magnetic field is applied, three additional invariants associated with the magnetic actuation vector $\mathbf{H}_\mathcal{L}$ are introduced:

$$\begin{aligned} I_4 &= \mathbf{H}_\mathcal{L} \cdot \mathbf{H}_\mathcal{L}, \\ I_5 &= (\mathbf{C}\,\mathbf{H}_\mathcal{L}) \cdot \mathbf{H}_\mathcal{L}, \\ I_6 &= (\mathbf{C}^2\,\mathbf{H}_\mathcal{L}) \cdot \mathbf{H}_\mathcal{L}. \end{aligned} \qquad (8)$$

Here, $\mathbf{H}_\mathcal{L}$ represents the magnetic actuation in the Lagrangian form and is defined as

$$\mathbf{H}_\mathcal{L} = J\mathbf{F}^{-1}\mathbf{H}\mu_0, \qquad (9)$$

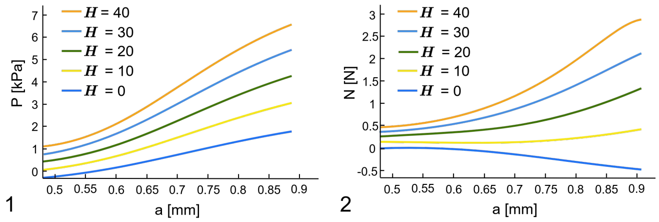

Fig. 2. (1) Pressure P versus inner radius a for different magnetic field magnitudes $|\mathbf{H}|$ [unit: mT]. (2) Tip force N versus inner radius a for the same field conditions. In both cases, $b/a = 1.125$ and $\lambda_z = 1$.

where $J = \det(\mathbf{F})$ and μ_0 is the vacuum magnetic permeability ($4\pi \times 10^{-7}$ N·A^{-2}).

For generality, we first consider the application of an internal pressure P on the inner surface $r = a$ and later set $P = 0$ to study pressure free growth. Because $\mathbf{H}$ is locally continuous across the inner and outer surfaces, its magnitude remains constant throughout the material. Consequently, the radial Maxwell stress is identical on $r = a$ and $r = b$, yielding an expression for P that as the same form as in the case of pure elasticity with a reduced energy function.

$$P = \mu(I_4) \int_a^b (\lambda_\theta^2 - \lambda_\theta^{-2}\lambda_z^{-2}) \frac{dr}{r}. \tag{10}$$

Fig. 2.1 illustrates the dependence of the pressure P on the magnetic field B. The pressure increases with the magnitude of the magnetic field. The eversion problem is thus fully defined after linking the axial stretch λ_z, the deformed inner radius a, and the tip-growing force N, given by

$$N_{\text{ideal}} = 2\pi\mu(I_4) \int_a^b \left[2\lambda_z^2 - \lambda_\theta^2 - \lambda_\theta^{-2}\lambda_z^{-2}\right] r\, dr + \pi a^2 P + \frac{\pi\mu_0}{2}(b^2 - a^2) I_4 (\lambda_z^2 - \lambda_z^{-2}). \tag{11}$$

The first two terms reduce to the classical neo-Hookean form in the absence of a magnetic field. The final term represents the contribution of the Maxwell stress, highlighting the magnetoelastic coupling. Notably, for $\lambda_z = 1$ and $P = 0$, we found $N < 0$, indicating that the magnetic field alone can induce eversion in the absence of any axial contact at the tip. Fig. 2.2 illustrates the variation of N with the outer radius a. For $\lambda_z > 1$, N increases and becomes positive, while for $\lambda_z < 1$ stability considerations arise and are beyond the scope of this study.

In the ideal model, the robot everts cleanly at the tip and material effectively "appears" outside without losses. In practice, as the robot grows, an increasing length of the tail slides against the inner wall, so internal contact and friction accumulate. Similarly to [18], we account for these losses by subtracting an equivalent drag term that represents tail–inner-wall sliding:

$$N = N_{\text{ideal}} - l\mu_k\, p_n(s) \phi\,(2\pi b)\, g(\Theta). \tag{12}$$

Here, l is the sliding contact length, μ_k is the kinetic friction coefficient, and $p_n(s)$ is the effective normal contact pressure between the moving tail and the surface it rubs on. The pressure $p_n(s)$ is assumed to be a fraction of the internal pressure P, captured by a contact factor $\alpha \in [0, 1]$ that represents how much of P is transmitted as normal load at the interface. The term $\phi(2\pi b)$ is the effective contact perimeter, where $\phi \in [0, 1]$ accounts for reductions in contact due to tail geometry (cylindrical or cruciform in this study).

In bent configurations, friction is further amplified by a capstan-like effect. Specifically, when the sliding material wraps along a curved path, the tension follows an exponential relation captured by

$$g(\Theta) = e^{(\gamma\, \mu_k\, \Theta)} \tag{13}$$

where Θ is the cumulative bending angle and $\gamma \in [0, 1]$ is a geometry factor (smaller for cruciform than for circular tails).

C. External Permanent Magnet (EPM) Poses

Magnetic profiles for shape forming have been extensively described in previous studies, and detailed optimization procedures to achieve target geometries can be found in [11], [19]. We adopt a discretization of the continuum structure using a pseudo-rigid-body model, in which bending is represented by a serial assembly of 2D springs characterized by stiffness parameters obtained from material characterization, while the rigid links are subjected to magnetic torques when external magnetic fields are applied.

A time-stepping optimization routine computes both the magnetic profile and the field sequence needed to achieve a follow-the-leader trajectory in the XY plan. Following [19], the field $\mathbf{H}$ generated by an external permanent magnet (EPM) is related to its pose using the magnetic dipole expansion as:

$$\mathbf{H} = \frac{\mu_0 |\boldsymbol{m}|}{4\pi |\mathbf{p}|^3} \left(3\hat{\mathbf{p}}\hat{\mathbf{p}}^{\mathrm{T}} - \mathbf{I}_3\right) \hat{\boldsymbol{m}}, \tag{14}$$

where $\mathbf{p} \in \mathbb{R}^3$ denotes the position vector of the EPM, and $|.|$ denotes the Euclidean norm, with $\hat{\cdot} = \frac{\cdot}{|.|}$.

Matching a desired $\mathbf{H}$ yields

$$|\mathbf{p}| = \left(\frac{2\pi |\mathbf{H}|}{\mu_0 |\boldsymbol{m}|}\right)^{\frac{1}{3}}, \tag{15}$$

$$\hat{\boldsymbol{m}} = \frac{\left(3\hat{\mathbf{p}}\hat{\mathbf{p}}^{\mathrm{T}} - \mathbf{I}_3\right)^{-1}}{|3\hat{\mathbf{p}}\hat{\mathbf{p}}^{\mathrm{T}} - \mathbf{I}_3|} \hat{\mathbf{H}}. \tag{16}$$

In our experiments, we additionally minimize the vertical component $H_{z|\text{EPM}}$ during optimization to avoid interference with the shape-sensing mechanism.

D. Shape Reconstruction from Magnetic Sensing

Assuming the optimized field distribution produces the intended deformation, we reconstruct the robot shape using embedded magnetic sensors. Soft magnetic markers are integrated on the outer wall and magnetized along the Z-axis, orthogonal to the primary steering magnetization.

Miniaturized 3D Hall-effect sensors are embedded along the camera cable in the robot's internal channel to detect the local magnetic field generated by these markers. The Z-axis magnetization aligns with sensor characteristics: the

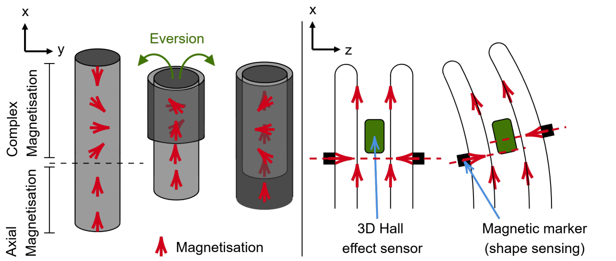

Fig. 3. (Left) After molding, the soft growing robot is magnetized in two sections—one with a complex magnetic profile and another axially magnetised, so that, once everted, its magnetic signature matches the optimised one for shape forming. (Right) During bending, the soft magnetic marker moves at a different speed relative to the magnetic sensor, changing their alignment as a function of the deformation amplitude.

saturation threshold along Z is 2.5 times higher than in X/Y, and safely above fields generated by our platform under clinical constraints (eg. a minimum distance of 15 cm between the patient and the EPM).

Markers are placed with a known 5 mm proximal offset relative to the sensors. As the robot bends in the XY-plane, one side undergoes extension while the opposite side experiences compression, changing the relative alignment between each marker and its corresponding sensor (Fig. 3). Increased bending aligns the marker with the sensor's sensitive axis, increasing H_z:

$$H_z \propto \beta, \tag{17}$$

where β is the local bending angle. The bending direction is identified by the sign of H_z: $H_z < 0$ for rightward bending and $H_z > 0$ for leftward bending.

Modeling a marker as a z-aligned dipole with moment m, sensor–marker axial gap h, and lateral offset ρ, the normal field H_z at the sensor is expressed as:

$$H_z(\rho, h) = \frac{\mu_0 m}{4\pi} \frac{2h^2 - \rho^2}{(\rho^2 + h^2)^{5/2}}, \tag{18}$$

which peaks at $\rho = 0$:

$$H_0 = H_z(0, h) = \frac{\mu_0 m}{2\pi h^3}. \tag{19}$$

By normalizing H_z with respect to H_0, we obtain a dimensionless ratio:

$$q = \frac{H_z}{H_0} = \frac{2 - (\rho/h)^2}{2(1 + (\rho/h)^2)^{5/2}}. \tag{20}$$

For $q > 0.7$, a closed-form approximation provides sufficient accuracy:

$$\rho \approx h\sqrt{\frac{1-q}{3}}, \tag{21}$$

where h is obtained via calibration.

Assuming the robot undergoes constant-curvature deformation for a segment of arc length L, the bending angle β, curvature κ, and radius of curvature r are related by:

$$\beta = \frac{L}{r}, \quad r = \kappa^{-1}, \quad \text{and} \quad \kappa = \frac{\rho}{Lh}, \tag{22}$$

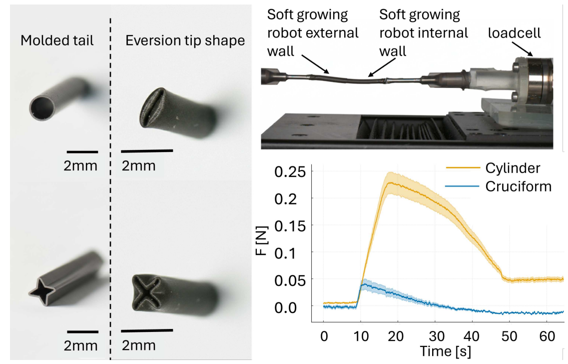

Fig. 4. Magnetic soft growing robot, molded and everted, with (left) cylindrical and cruciform tails. (Top right) Setup to characterize pulling force versus tail shape. (Bottom right) Resulting force–displacement curves.

Under the constant-curvature assumption, any point along the robot's neutral axis can be described in Cartesian coordinates as:

$$\xi = \begin{bmatrix} r(1 - \cos\beta) & 0 & r\sin\beta \end{bmatrix}^{\mathrm{T}}. \tag{23}$$

We display the reconstructed arcs in a custom graphical user interface (GUI) for real-time feedback.

III. Implementation

A. Magnetic Soft Growing Robot Fabrication

The magnetic soft growing robots were fabricated by mixing Dragon Skin 10 (Smooth-On Inc., USA) with NdFeB microparticles in a 1:1 mass ratio. The composite mixture was prepared and degassed using a high-vacuum mixer (ARV-310, THINKY MIXER, Japan) operating at 2000 rpm for 90 s. The degassed mixture was then injected into a 3D-printed mold (HTL resin, microArch S140, BMF, USA). To avoid damaging the thin 100 μm wall, the mold was dissolved in an acetone bath immediately after curing. Although thinner walls are achievable (down to half the reported thickness), we observed the onset of kinking rather than smooth, continuous deformation without pressure; therefore, we retained the nominal thickness reported here.

To assign the magnetic signature along X and Y, cured cylinders were placed in 3D-printed trays and magnetized under a saturating uniform field of 4.644 T (ASC IM-10-30, ASC Scientific, USA). The first half of each magnetic soft growing robot was magnetized with a spatially varying profile for controlled bending, while the second half was magnetized axially to minimize self-attraction between walls, which would otherwise hinder eversion.

Magnetic markers for shape sensing were made from the same silicone but doped to 200% NdFeB (by mass) to compensate for their reduced size. These segments were magnetized along Z and bonded using Sil-Poxy (Smooth-On Inc., USA).

A key advantage of a soft growing robot is its built-in central channel, which can house instrumentation. We embedded a miniature camera (NanEye, ams-OSRAM, USA) and two 3D Hall-effect sensors (AK09973D, Asahi Kasei Microdevices/AKM) mounted along the camera cable. The sensors were read over an I^2C protocol by a microcontroller

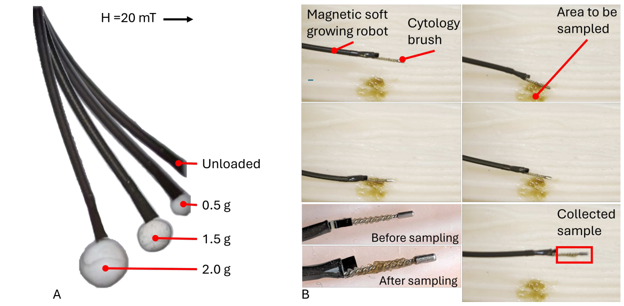

Fig. 5. (A) Overlays of the magnetically actuated soft growing robot bending in-plane under varying tip loads. (B) Benchtop demonstration of simulated biopsy-sample collection via magnetic manipulation of the soft robot.

(Teensy 3.6, PJRC, USA), which streamed the data to the main computer via ROS Serial at 500 Hz. The sensing assembly was motorized and synchronized with growth using a five-phase hybrid stepper (MS17HV, MOONS'), a digital driver (2DM542, Just Motion Control), and a microcontroller (Arduino UNO R4 Minima, Arduino). Internal surfaces were lubricated with silicone oil prior to deployment to reduce friction during shape forming.

B. Procedure for friction and stiffness characterization

Without internal pressure, the everted walls remain in contact, increasing internal friction and impeding eversion. We compared a standard cylindrical tail with a cruciform cross-section (Fig. 4). Although the cruciform section everts toward a near-cylindrical shape, its uneverted tail retains the star geometry, reducing contact area. We also assessed the effect of tail geometry on structural stiffness.

Rather than a full tribological study, that would be beyond the scope of this study, we performed a simplified pulling-force test. We collected 20 mm segments of everted robots, with the tail inside the outer wall. The tail section was fixed to a load cell (F/T Nano17 Ti, ATI, USA) mounted on a linear stage (NRT150, Thorlabs, USA), while the external wall was secured to a fixed base as illustrated in Fig. 4, top right. The load cell was translated at 0.2 mm/s, and the pulling force was recorded. Higher force values indicates higher internal friction. The forces were measured over five repetitions for both designs, and the results are presented in Fig. 4, bottom right. No lubrication was used during this experiment.

We then characterized the lateral and vertical stiffnesses by applying a crushing force on the everted robot, using the same setup components that were previously described. The loadcell was positionned in contact with the sample then moved at 0.2 mm/s over a 1.5 mm displacement. Lateral and axial (vertical) stiffnesses were then characterized by compressing the everted robot using the same setup. The load cell contacted the sample and advanced at 0.2 mm/s over a 1.5 mm displacement. Lateral stiffness was measured along both principal planes, as tip eversion shape induce asymmetry. In both lateral and axial tests, stiffness was computed from the peak force over the imposed displacement. All characterizations were repeated five times.

To demonstrate that the robot can be maneuvered to a target area and that it is sufficiently stiff to generate the normal force required for biome sampling without buckling or retracting, we performed two experiments illustrated in Fig. 5. First, we conducted a load–deformation characterization using a 1D Helmholtz coil (DXHC10-200, Dexing Magnet Tech. Co., Ltd., Xiamen, China). Different tip loads, ranging from 0 to 2 g were applied sequentially while maintaining a constant magnetic field of 20 mT for comparison. Second, we conducted a benchtop demonstration in a silicone phantom. A gelatin layer was placed over a region of interest to emulate a soft tissue surface, and the robot was magnetically steered to manipulate the brush and collect a simulated sample.

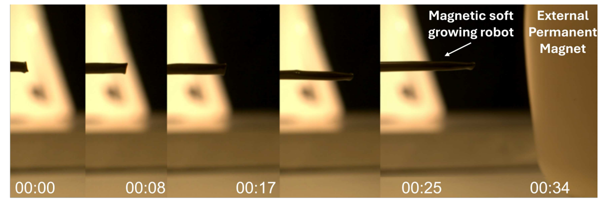

Fig. 6. Snapshots of pressure-free growth under an axial magnetic field generated by the external permanent magnet.

C. Pressure Free Growing Process

To validate the proposed model for magnetically induced eversion and pressure-free growth, we employed a large EPM to generate an axial field and observed the resulting deployment (Fig. 6). The EPM had a cylindrical shape, and measured 101.6 mm in diameter and length, and an axial magnetisation of 970.1 Am^2 (Grade N52). It was fixed on a 7-DOF serial robotic manipulator (LBR iiwa14, KUKA, Germany) in order to steer the magnetic soft growing robot. Due to the relatively low concentration of NdFeB microparticles within the composite structure, the magnetic response is relatively weak; thus, the robot must be positioned close to the EPM to achieve growth solely under magnetic actuation. Despite this, we demonstrate pressure-free eversion, confirming the model's prediction. Experimentally, magnetic growth requires a minimum field magnitude of 43 mT. With lubrication (e.g., silicone oil), reliable growth can be achieved with the EPM positioned 7 cm from the robot. In practice, the initial deployment can be assisted with a low pneumatic pressure (0.1 kPa), after which steering is provided magnetically.

Following the demonstration introduced in [8], we also show that the robot can be manipulated using similar magnetic strategies. Specifically, torque-dominated actuation (Fig. 7.A) is obtained by orienting the EPM such that its magnetization axis is orthogonal to that of the soft magnetic growing robot, creating a magnetic misalignment that generates torque. In contrast, force-dominated actuation (Fig. 7.B) is achieved by exploiting the magnetic-field gradient, by aligning the EPM magnetization axis with that of the soft magnetic robot to generate a net magnetic force.

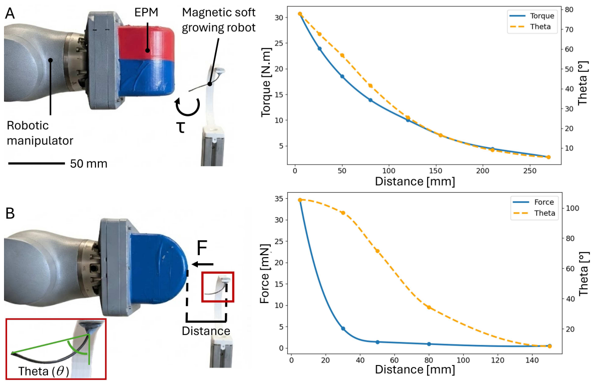

Fig. 7. Illustration of the two actuation modes used depending on the robot–EPM orientation: (A) torque-dominated actuation and (B) force-dominated actuation. Right: corresponding plots of the magnetic torque (τ) or force (F) applied by the EPM and the resulting deflection angle θ as a function of distance.

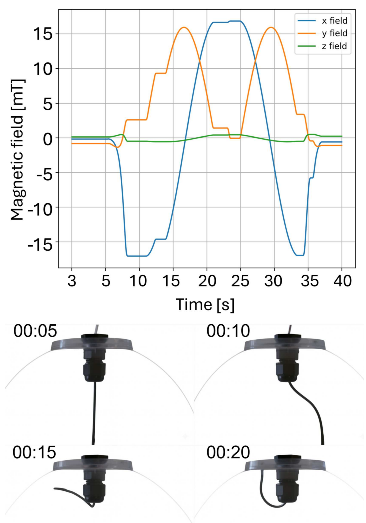

Fig. 8. Illustration of the shape forming by retroflexion. (Left) Planning output enforcing negligible Z-field. (Right) Snapshots of intermediate configurations culminating in full retroflexion.

D. Distributed Shape Forming (Retroflexion)

Unlike prior magnetic soft growing robots, which often limit control to distal tip steering or require additional lateral structures, our design enables distributed actuation along the body. We designed the first magnetic profile to achieve full retroflexion, to showcase dexterity and to demonstrate a clinically relevant capability. The EPM was maneuvered according to the optimized sequence, and the robot transitioned through intermediate configurations that reduced the Z-field component, as planned (Fig. 8). In contrast to [8], removing the inextensible layer suppresses wrinkling and creasing instabilities and enables a continuous deformation. We demonstrated retroflexion in a fresh ex vivo porcine stomach by deploying and retroflexing the robot (Fig. 10A), and then performing cytology brush sampling through the inner channel (Fig. 10B; see supplementary video).

E. Real-Time Shape Sensing and Reconstruction (S-Shape)

In the retroflexion case, the curvature is constant along the entire length; therefore, we focus on S-shaped deformation, which better demonstrates the shape-sensing capability. While the operator is moving the EPM, the GUI provides a live reconstruction. The nominal H_{z0} is measured after fabrication for each robot and stored. A quick operator calibration (bending $\pm 90°$) initializes readings and compensates for any sensor shift during growth. Steering with the EPM yields the target deformation and real-time rendering (Fig. 9). To validate this approach, we quantified the deviation between the experimentally measured shape, given by the extracted centerline, and the shape reconstructed by the model. The centerline was extracted by background subtraction using a threshold mask, then skeletonizing the object to a one-pixel-wide line.

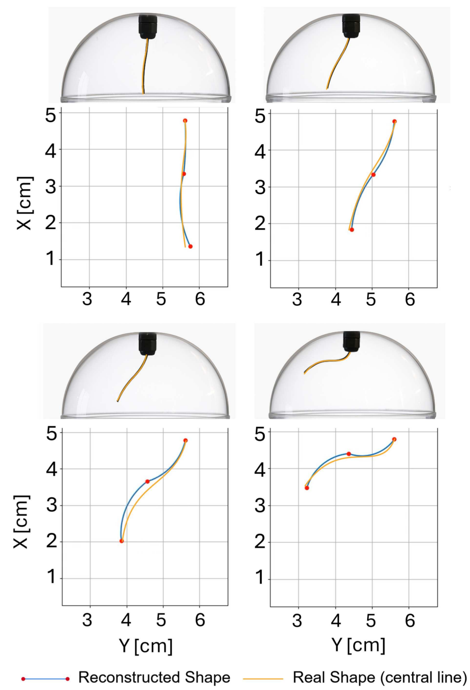

Fig. 9. S-shaped deformation with real-time shape reconstruction using magnetic sensing. After the experiment, the robot's centreline was extracted from video and compared with the shape reconstructed from measured magnetic-field variations.

IV. RESULTS AND DISCUSSION

We first analyze friction and stiffness as a function of tail shape. As illustrated in Fig. 4, the cruciform shape reduces the required pulling force by a factor of five, making it clearly advantageous for pressure free growth. Starting from a cylindrical tail, lateral structural stiffness is asymmetric and depends on the fold direction; representative stiffnesses are 121 and 68 N/m along the two orthogonal directions. In contrast, the cruciform tail yields more uniform lateral stiffness of approximately 147 N/m along both axes. Axially, the cylindrical tail exhibits buckling below $\sim$ 600 N/m, whereas the cruciform tail withstands up to $\sim$ 950 N/m. Thus, tail shape affects both friction and stiffness, with a clear advantage for the cruciform design in the pressure-free regime. Pressure-free growth is attractive in scenarios where pressurization is undesirable or impractical. However, as demonstrated it requires relatively high magnetic fields and yields slower growth. These limitations are primarily attributable to friction that must be overcome, which is particularly significant at the millimeter-scale, as well as to material inhomogeneities or insufficient magnetic particle loading resulting from manual fabrication. In the first case, the model could be refined through an extensive tribological study to enable more accurate parametrization of friction coefficients and tail–inner-wall contact mechanics. In the second case, adopting an industrial injection-moulding process, together with increased magnetic particle loading, and using a larger and higher-grade external permanent magnet (e.g., N57), should enable operation at a larger distance between the EPM and the soft robot, thereby helping to ensure a minimum separation for patient safety [20]. Retraction was not considered in this study. Modelling retraction requires extending the formulation to $\lambda_z < 1$, where stability issues and buckling may occur. Future work should therefore consider actuation strategies that generate a more homogeneous magnetic field, for instance using two external permanent magnets or electromagnets. In our third experiment, we demonstrate real-time 2D shape control while maintaining the magnetic field primarily in the XY-plane and minimizing the Z component (Fig. 8). Bench-top fields up to 25 mT are used, in line with clinical considerations [19], and we demonstrate ex vivo stomach exploration and sampling (Fig. 10). Finally, we provide real-time shape sensing with user feedback of the reconstructed shape. The resulting root-mean-square error (RMSE) is 2.7 mm. The largest errors occur when β changes sign (from positive to negative or vice versa). This is consistent with a dead-zone–like behavior in cable actuation, whereby the signal at small angles becomes indistinguishable from background noise. Some loss of smoothness is observed and visible in the supplementary video, likely due to deviations from the constant-gap assumption between sensors and markers. Maintaining this gap is challenging; low pressurization could help, but it would stiffen the robot and reduce the available workspace.

V. Conclusion

We presented in this paper a model that links hyperelastic and magnetic properties during eversion and demonstrated pressure-free growth in practical scenarios. Leveraging material intelligence, via spatial magnetization profiles and hyperelasticity, we achieved distributed shape forming and real-time shape sensing under carefully controlled magnetic fields of a 1.8 mm diameter magnetic growing soft robot. We further validated these capabilities ex vivo in fresh tissue, demonstrating endoscopic exploration and cytology brush sampling, suggesting a path toward real-world applications.

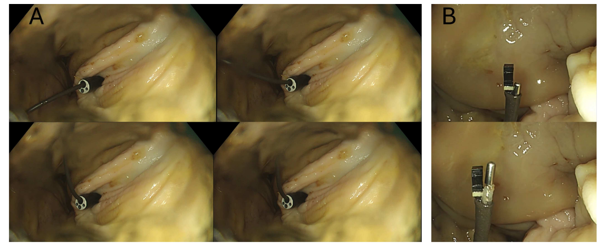

Fig. 10. Ex vivo demonstration. (A) Retroflexion during gastric exploration. (B) Sample collection with a cytology brush through the inner channel.

References

[1] L. H. Blumenschein, M. M. Coad, D. A. Haggerty, A. M. Okamura, and E. W. Hawkes, "Design, modeling, control, and application of everting vine robots," *Frontiers in Robotics and AI*, 2020.

[2] S. Al Harthy, S. H. Sadati, C. Girerd, S. Kim, A. Mondini, Z. Wu, B. Saldarriaga, C. A. Seneci, B. Mazzolai, T. K. Morimoto, and C. Bergeles, "Tip-growing robots: Design, theory, application," *IEEE Transactions on Robotics*, vol. 41, pp. 5511–5532, 2025.

[3] J. D. Greer, T. K. Morimoto, A. M. Okamura, and E. W. Hawkes, "A soft, steerable continuum robot that grows via tip extension," *Soft Robotics*, vol. 6, no. 1, pp. 95–108, 2019.

[4] P. Berthet-Rayne, S. M. H. Sadati, G. Petrou, N. Patel, S. Giannarou, D. R. Leff, and C. Bergeles, "Mammobot: A miniature steerable soft growing robot for early breast cancer detection," *IEEE Robotics and Automation Letters*, vol. 6, no. 3, pp. 5056–5063, 2021.

[5] Z. Bi, T. Ji, S. Dogramadzi, S. J. L. Phee, J. Liu, W. Lai, D. Wu, B. Zhang, and L. Cao, "Hysteresis-assisted shape morphing for soft continuum robots," *Science Advances*, p. eadx3024, 2025.

[6] S. Kim, G. Dong, A. Mangan, D. Agrawal, S. Cai, and T. K. Morimoto, "Lce-integrated soft skin for millimeter-scale steerable soft everting robots," *Science Advances*, vol. 11, no. 42, p. eadw8636, 2025.

[7] J. Davy, T. P. Dean, N. J. Greenidge, B. Calmé, P. Lloyd, J. H. Chandler, and P. Valdastri, "Magnetic fluid-driven vine robots for minimally invasive tissue biopsy sampling," *Advanced Intelligent Systems*, 2025.

[8] J. Davy, N. J. Greenidge, S. Kim, L. J. Tinsley, P. Lloyd, J. H. Chandler, R. A. Harris, T. K. Morimoto, and P. Valdastri, "Vine robots with magnetic skin for surgical navigations," *IEEE Robotics and Automation Letters*, vol. 9, no. 8, pp. 6888–6895, 2024.

[9] N. G. Kim and J.-H. Ryu, "A soft growing robot using hyperelastic material," *Advanced Intelligent Systems*, vol. 5, no. 2, 2023.

[10] K. Yoonho, Y. Hyunwoo, Z. Ruike, A. C. Shawn, and Z. Xuanhe, "Printing ferromagnetic domains for untethered fast-transforming soft materials," *Nature*, vol. 558, pp. 274–279, 2018.

[11] P. Lloyd, G. Pittiglio, J. H. Chandler, and P. Valdastri, "Optimal design of soft continuum magnetic robots under follow-the-leader shape forming actuation," in *2020 International Symposium on Medical Robotics (ISMR)*, 2020, pp. 111–117.

[12] R. S. Rivlin, "Large elastic deformations of isotropic materials vi. further results in the theory of torsion, shear and flexure," *Philosophical Transactions of the Royal Society of London*, pp. 173–195, 1949.

[13] D. Haughton and A. Orr, "On the eversion of compressible elastic cylinders," *International Journal of Solids and Structures*, 1997.

[14] F. Przybylski, Y. Adagolodjo, A. Mira, G. Cerruti, J. Dequidt, C. Duriez, and P. Berthet-Rayne, "3d kinematics and quasi-statics of a growing robot eversion," in *2023 IEEE International Conference on Soft Robotics (RoboSoft)*, 2023, pp. 1–6.

[15] S. R. Goldstein, R. E. Jones, J. J. Sipe, J. L. Doppman, and J. W. Boretos, "A miniature toposcopic catheter suitable for small diameter tortuous blood vessels," *Journal of Biomechanical Engineering*, 1980.

[16] Y. Feteih, S. Kim, and T. K. Morimoto, "Active stiffening for vine robots via axially stacked pneumatic pouches," in *2025 IEEE 8th International Conference on Soft Robotics (RoboSoft)*, 2025.

[17] T. Baaij, M. K. Holkenborg, M. Stölzle, D. Van Der Tuin, J. Naaktgeboren, R. Babuška, and C. Della Santina, "Learning 3d shape proprioception for continuum soft robots with multiple magnetic sensors," *Soft Matter*, vol. 19, no. 1, pp. 44–56, 2023.

[18] C. Girerd, A. Alvarez, E. W. Hawkes, and T. K. Morimoto, "Material scrunching enables working channels in miniaturized vine-inspired robots," *IEEE Transactions on Robotics*, vol. 40, pp. 2166–2180, 2024.

[19] B. Calmé, A. Metcalf, M. Brockdorff, H. Jang, Y. Choi, P. Lloyd, S. C. Ryu, and P. Valdastri, "Hybrid tendon-actuated and soft magnetic robotic platform for pancreatic applications," *IEEE Robotics and Automation Letters*, vol. 10, no. 2, pp. 1784–1791, 2025.

[20] B. Calmé, N. J. Greenidge, A. Metcalf, A. Bacchetti, G. Loza, D. Kpeglo, P. Lloyd, V. Pensabene, J. H. Chandler, and P. Valdastri, "Moving beyond compliance in soft-robotic catheters through modularity for precision therapies," 2026. [Online]. Available: https://arxiv.org/abs/2601.14837